Metal-doped imine frameworks for the oxygen reduction reaction in acidic media

Álvaro Tolosana-Moranchel [a,**], Álvaro García [a], Álvaro García-Corral [b,c], José F. Marco [d], L. Pascual [e], Dalia Liuzzi [a], Mohamed A. Salam [f], Pilar Ferrer [g], Jorge Torrero [c], David C. Grinter [g], Georg Held [g], Daniel García Sánchez [c], K. Andreas Friedrich [c,h], María Retuerto [a], Sergio Rojas [a,*]

[a] Grupo de Energía y Química Sostenibles, Instituto de Catálisis y Petroleoquímica, CSIC. Marie Curie 2, 28049, Madrid, Spain
[b] Dept. Física Matemática y de Fluidos, Universidad Nacional de Educación a Distancia, Avda. Esparta S/n, 28232, Las Rozas, Spain
[c] Institute of Engineering Thermodynamics/Electrochemical Energy Technology, German Aerospace Center (DLR), Pfaffenwaldring 38-40, 70569, Stuttgart, Germany
[d] Instituto de Química Física "Rocasolano", CSIC, Serrano 119, 28006, Madrid, Spain
[e] Instituto de Catálisis y Petroleoquímica, CSIC. Marie Curie 2, 28049, Madrid, Spain
[f] Chemistry Department, Faculty of Science, King Abdulaziz University, P. O Box 80200, Jeddah, 21589, Saudi Arabia
[g] Diamond Light Source, Harwell Science and Innovation Campus, Didcot, OX11 0DE, UK
[h] University of Stuttgart, Institute of Energy Storage, Pfaffenwaldring 31, 70569, Stuttgart, Germany

HIGHLIGHTS

- A high N/C ratio precursor such as melamine used to synthesize Fe–N–C catalysts.
- FeN_4C_{10} and FeN_4C_{12} moieties formed during the synthesis.
- Site Density of exposed Fe sites determined by in situ and ex situ analyses.
- ORR activity demonstrated in RDE and MEA configurations.

GRAPHICAL ABSTRACT
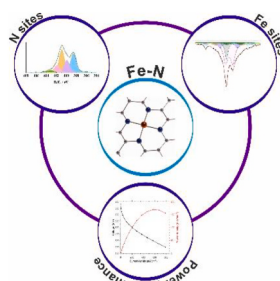
ABSTRACT

The overall performance of proton exchange membrane fuel cells is limited by the sluggish kinetics of the oxygen-reduction reaction (ORR). Among the most active PGM-free ORR electrocatalysts are metal-nitrogen-carbon (M-N-C), such as Fe–N–C. The Fe–N_4 ensembles in these PGM-free catalysts, present in different configurations, are proposed to be the active sites for the ORR in acid. In this work, we have synthesized a Fe/N/C catalyst via thermal treatment of a polymeric C_xN_y precursor obtained by the wet-polymerization of melamine (a nitrogen rich molecule) and terephthaldehyde. The materials obtained (Im-FeNC-1HT and Im-FeNC-2HT) display high ORR activity in acid electrolyte compared to other Fe–N–C catalysts prepared with precursors different than 2-methylimidazole or ZIF-8. Characterization data indicate the formation of high- and low-spin Fe-N_x ensembles, with a site density of $4.4 \cdot 10^{19}$ sites$_{Fe} \cdot g^{-1}$ estimated by electrochemical stripping of NO. The ORR activity was evaluated in a RRDE configuration in 0.1 M HClO$_4$ and in MEA configuration in a single cell.

1. Introduction

The current energy model, based on the burning of fossil fuels, is perceived as a major risk to sustainable development. Equally important, it entails the energy dependence on foreign, sometimes unstable countries, resulting in strong geopolitical tensions. That is why the European Union has set a pathway to reach climate neutrality by 2050 [1]. In order to achieve this goal, we must follow an energy transition to replace fossil fuels with renewable energy. Green hydrogen, a term coined to identify the hydrogen produced from clean energy sources, is currently considered as a versatile energy vector that will be crucial to decarbonize several hard-to-decarbonize sectors such as transportation, heating and power for buildings or industry and steel production. The transportation sector is already changing into a better perspective of the world-wide future, trying to become a zero-emission industry. In order to reduce the CO_2 emissions in vehicles, two main alternatives are in current development: batteries and fuel cells (FCs) [2]. Fuel cell technology relies on external factors, namely, the large-scale production and distribution network of green hydrogen and the research aimed at reducing the platinum amount in the electrodes or replace it by a catalyst free of platinum-group metals (PGMs) [3–5].

Fuel cells generate electrical energy by recombining hydrogen and oxygen in water as a main product. A fuel cell consists of two electrodes, namely, the anode, where H_2 oxidizes into H^+ releasing electrons via the hydrogen-oxidation reaction (HOR), and the cathode, where O_2 is reduced via the oxygen-reduction reaction (ORR) to produce water. State-of-the-art proton-exchange membrane (PEM) FCs commonly use Pt-based catalysts on both electrodes, with higher loadings of Pt at the cathode [2]. Even though Pt works effectively, it also involves important drawbacks such as its high price, global scarcity and long-term corrosion [6]. Current research efforts on the ORR are focused on the development of novel catalysts made of more abundant materials.

The most advanced alternative to Pt-based catalysts for the ORR are the so-called non-precious metal catalysts, in which a single transition-metal atom is stabilized within a nitrogen doped carbon matrix. The most common transition metals are iron and cobalt because they show better results than others in terms of activity and durability [7]. These FeC_xN_y ensembles contains different $Fe-N_y$ moieties, which can participate in the ORR to a different extent. Although there is some controversy regarding the nature of the active sites, it is generally accepted that the FeN_4 sites are the most active ones for the ORR in acid [7–11]. Recent studies have gone further and identified high-spin $O_2–Fe(III)N_4C_{12}$ and low-spin $Fe(II)N_4C_{10}$ moieties to be the active sites for the ORR [12], with the former species displaying higher initial ORR activity, but lower stability than $Fe(II)N_4C_{10}$ [11,13].

The synthesis of Fe/N/C catalysts usually comprises several common steps: firstly, a mixture of iron, nitrogen and carbon precursors are mixed and subjected to one or more thermal treatments under flow of an inert or reactive gas (NH_3) at high temperature (between 600 °C and 1100 °C). Then, acid leaching of the pyrolyzed catalyst is carried out to remove spectator phases including metallic Fe, iron oxides, Fe_3C and other metals used during the synthesis such as Zn particles. Lastly, another thermal treatment is further applied. The current research of new electrocatalysts englobes these common aspects coupled to a series of trial-and-error selection of precursors (metals, monomers and supports) and modifications of morphology and structure [14–16]. The most active catalysts obtained to date are produced from a Zn-containing zeolite imidazole framework (ZIF-8) mixed (either via wet or solid-state chemistry) with a nitrogen precursor such as 1,10 phenanthroline and an iron source, typically $FeCl_3$, Fe_2O_3 or others. In order to obtain the final catalyst, the mixture is subjected to one or several thermal treatments, usually followed by an acid leaching step and a further thermal treatment [10,11,17,18]. Other approaches in the literature focuses on the pyrolysis of molecular precursors with a high N/C ratio and high surface area, typically C–N-frameworks such as covalent organic frameworks (COFs) or covalent triazine frameworks

(CTFs) [19–21]. These are usually prepared by wet or dry polymerization of carbon and nitrogen precursors such as dicyanobenzenes under controlled conditions, resulting in Fe/N/C catalysts for the ORR [22]. Among these frameworks, Melamine (2,4,6-Triamino-1,3,5-triazine) could be a suitable precursor for the synthesis of atomically dispersed Fe/N/C catalysts for the ORR since it contains a high fraction of nitrogen atoms in its structure (N/C = 6/3), establishing as a very low-cost precursor.

Recent studies have successfully demonstrated the feasibility of C–N-based materials as valid catalyst precursors: on one hand, Liu et al. have reported the synthesis of a covalent S,N-based organic polymer for the capture of CO_2 and iodine from the one-pot polymerization of thiophene and melamine [23] and Sang et al. reported the synthesis of a N-rich porous organic polymer with high surface area, using melamine as the nitrogen precursor via a Schiff base reaction mechanism [24]. On the other hand, melamine has already been used as a precursor for the synthesis of Fe/N/C catalysts triggering the ORR in PEMFC environments, for instance via the production of N-containing aerogels [25], in the form of cyanamide [26] or by using it in the presence of other N-containing precursors. In this work, we have synthesized a novel Fe/N/C catalyst using melamine as the nitrogen source via the polymerization of melamine and terphthaldehyde. A N-rich imine-based framework was synthesized from the wet-polymerization of melamine and terephthaldehyde, followed by the addition of $Zn(NO_3)_2$ and Fe $(NO_3)_3$. The material obtained was used as a precursor for the synthesis of Fe/N/C via thermal treatments under controlled atmosphere. The structure, composition, and morphology of the catalysts obtained has been determined by a combination of different techniques, including ^{57}Fe Mössbauer spectroscopy, XPS, XRD and BET. The quantification of the active sites has been conducted by both *ex-situ* CO cryo-chemisorption and *in-situ*, nitrite reduction stripping. Catalytic performance has been characterized in a rotating-disk-electrode (RDE) and demonstrated in membrane-electrode-assembly (MEA) configuration.

2. Experimental section

2.1. Synthesis of Im-FeNC

The chemicals used in the synthesis of the Im-FeNC catalyst were purchased from Sigma Aldrich except for the iron (III) nitrate that was purchased from Alfa Aesar. Firstly, the desired quantities of melamine and terephthaldehyde were dissolved in 120 mL of dimethyl sulfoxide (DMSO) in a flask under inert atmosphere with a water reflux system [27,28]. Once the mixture is completely homogeneous at 30 °C, Zn $(NO_3)_2$ and $Fe(NO_3)_3$ were added gently to the solution. The mixture was stirred and heated to 180 °C for 16 h under an inert atmosphere, obtaining a yellowish solid, which was filtered, washed with excess of acetone and dried overnight. The resulting material was subjected to a thermal treatment at 900 °C using a 20 °C/min ramp under a N_2 flow of 450 NmL/min. After 110 min at 900 °C, NH_3 was flown in the reactor (N_2/NH_3 = 450/70 NmL/min), during 30 min. The material obtained after the first pyrolysis was labelled as Im-FeNC-1HT. Then, this catalyst was acid-leached in 2 M H_2SO_4 during 8 h at 70 °C, in order to remove metallic Fe phases. Finally, the catalyst was subjected to a second pyrolysis following the same aforementioned steps. The catalyst obtained was named as Im-FeNC-2HT. Scheme 1 depicts an illustration of the key steps during the synthesis of the catalysts.

2.2. Catalyst characterization

The crystal structure of the catalysts was analyzed with an X-ray polycrystal PANalytical X'Pert PRO using nickel-filtered CuK_α (1.541874 Å) radiation, with a 0.04° step size and accumulating 20 s per point.

Raman spectroscopy was used to analyze the graphitic structure of
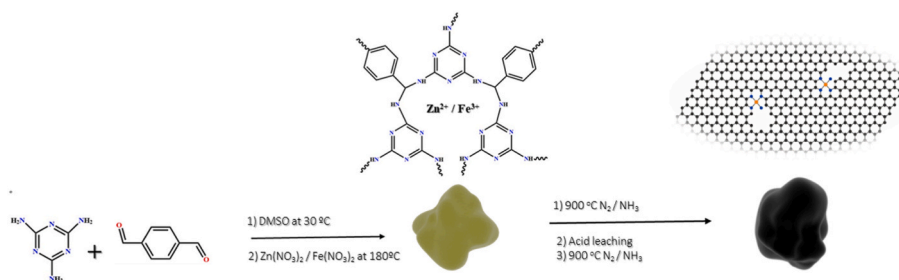
Scheme 1. Synthesis of Fe/N/C. A yellowish solid is obtained from the polymerization of melamine and terephthalaldehyde in the presence of $Zn(NO_3)_2$ and Fe $(NO_3)_3$. Fe/N/C catalysts obtained from the pyrolysis, acid leaching and pyrolysis of such polymer.

the catalysts. The spectra were recorded with a Renishaw Micro Raman spectrometer ($\lambda = 532$ nm) equipped with a 20 mW He–Ne laser emitting at 532 nm. Spectra were recorded using 3 repetitions, 10 s of acquisition time and 0.2 mW of incident power.

Surface area and pore size distribution of the samples were acquired by N_2 adsorption/desorption isotherm (relative pressure range $P/P_0 = 0.05–0.30$). The measurements were done at 77 K (nitrogen boiling point) in a Micrometritics Micromeritics ASAP 2000. The samples were degassed at 140 °C under vacuum for 24 h.

Transmission Electron Microscopy (TEM) data was recorded on a JEOL 2100 field emission gun transmission electron microscope operating at 200 kV and equipped with an EDX spectrometer Oxford INCA Energy 2000 system. Specimens were prepared by depositing small portions of the samples on top of a Cu grid supporting a lacey carbon film. Deposition was achieved by preparing a suspension of the material in ethanol.

^{57}Fe Mössbauer spectra were recorded at room temperature and 8.5 K in the transmission mode using a conventional constant acceleration spectrometer and a ^{57}Co(Rh) source. The velocity scale was calibrated using a 6 μm thick α-Fe foil. All the spectra were computer-fitted and the chemical isomer shifts were referred to the centroid of the spectrum of α-Fe at room temperature.

X-ray photoelectron spectroscopy experiments were performed at Versatile Soft X-ray (VerSoX) beamline B07 B branch endstation 1 at Diamond Light [29,30]. The VerSoX B branch endstation1 is equipped with a PHOIBOS150 2D CCD hemispherical electron energy analyzer, operating at 60° off the synchrotron beam. The spectra were collected with a photon energy of 600 eV and energy was calibrated with the Au 4f peak. The XPS spectrum of the Fe 2p core-level were recorded using a SPECS customized system equipped with a non-monochromatic X-ray source XR 50 and a hemispherical energy analyzer PHOIBOS 150. X-ray MgK line (1253.6 eV) was used as excitation (operating at 200 W/12 kV). The energy regions of the photoelectrons of interest were scanned at increments of 0.1 eV and fixed pass energy of 20 eV. For the analyses, the C 1s core-level peak was set at 284.6 eV. Spectra were analyzed with the CasaXPS software using a Shirley background and Gaussian-Lorentzian line shape.

2.3. Electrochemical tests in rotating-disk electrode

To measure the ORR performance of the Im-FeNC catalysts an Autolab PGSTAT320 N potentiostat/galvanostat controlled by NOVA 2.1 software was used. Measurements were performed using a three-electrode set-up. The electrocatalyst was deposited on a Rotating Disk Electrode (RDE, Pine Instruments), with a mirror polished glassy carbon disk electrode of 5 mm of outer diameter. Unless otherwise stated, a catalyst loading on the electrode of 0.6 mg cm^{-2} was used. The ink was prepared by dispersing the catalyst in a mixture of ultrapure water (MilliQ 18.2 MΩcm), isopropanol and Nafion® 117 solution (5%) with a volume ratio of 1:1:0.052, to a final catalyst concentration of 6 mg mL^{-1}. This ink was sonicated with an ultrasonic tip and an ultrasonic bath for at least 10 min before it was placed onto the glassy carbon. When Pt/C

(Johnson Matthey, Pt/C 40 wt%) was used as a benchmark the mass loading was 0.4 mg cm^{-2}. The reference and counter electrode were Ag/AgCl (3 M) and a graphite rod respectively. In order to correct the Ag/AgCl scale to the RHE scale, the hydrogen evolution reaction was measured using a Pt wire as working electrode. Potentials are reported vs the reversible hydrogen electrode (RHE) after iR correction (resistance of 24 Ω in 0.1 M HClO$_4$ measured by electrical impedance spectroscopy at open voltage).

Before recording the ORR polarization curves, the catalyst was conditioned by recording several cyclic voltammograms between 0.05 and 1.2 V in Ar-saturated 0.1 M HClO$_4$ at 10 mVs^{-1}. Subsequently, the electrolyte was fully saturated of O$_2$ and the ORR polarization curves were obtained by recording CVs at 10 mVs^{-1} and 1600 rpm between 0.05 and 1.2 V. Once the ORR curves were collected, a blank voltammogram was recorded in Ar-saturated electrolyte under the same experimental conditions but without rotation. Pure Faradaic currents were obtained by subtracting the anodic sweeps of the ORR curve from the positive going branch of the blank voltammogram.

The production of hydrogen peroxide during the ORR was studied with a rotating ring disk electrode (RRDE) with a platinum ring and a disk area of 0.2375 cm^2. The potential of the Pt ring was set at 1.2 vs RHE to ensure the oxidation of the H$_2$O$_2$ produced during the ORR but preventing the oxidation of water [31]. The following equation was used to calculate the amount of H$_2$O$_2$ produced:

$$\% \, H_2O_2 = \frac{\frac{2 \cdot i_R}{N}}{i_D + \frac{i_R}{N}} \tag{Eq. 1}$$

where i_R and i_D correspond to the ring current and disk current respectively and N is the collection efficiency of the ring (38%).

Stability was evaluated by performing load cycle accelerated stress tests (AST) in Ar- or O$_2$-saturated 0.1 M HClO$_4$. For the AST, a potential program consisting on square-wave cycles between $E_1 = 0.6$ V during 3 s and $E_2 = 0.925$ V during 3 s, was applied. ORR polarization curves were collected at the beginning of the test (BoT) and after certain number of cycles.

2.4. Quantification of active sites

The mass site density (SD$_{mass}$) of the catalysts was determined from *in-situ* nitrite stripping experiments, following a protocol reported by Kucernak's group [32–34]. Experiments were carried out using the same set-up described for the electrochemical tests. However, in this case a 0.5 M acetate buffer of pH 5.2 (prepared with sodium acetate and glacial acetic acid) was used as electrolyte. Briefly, (1) the working electrode was cleaned by performing 20 scans at 100 mV s^{-1} and 10 scans at 10 mV s^{-1} between 1.05 V and −0.4 V in Ar-saturated electrolyte. Afterwards, the working electrode was subjected to 6 cycles at 10 mV s^{-1} between the same potentials in O$_2$-saturated acetate buffer. This protocol was repeated as many times as necessary until stable cyclic voltammograms were obtained. (2) Next, the ORR performance (of the unpoisoned electrode) was measured. CV scans were carried out at 10

mV s^{-1} and 1600 rpm between 1.0 and 0.3 V in O$_2$-saturated and in Ar-saturated electrolytes subsequently (to correct the ORR). Then, the baseline stripping CV was recorded at 10 mV s^{-1} and 1600 rpm between 0.4 and 0.6 V in Ar-saturated acetate buffer. (3) Afterwards, the working electrode was poisoned by washing it in a 0.125 M NaNO$_2$ solution at OCP and 300 rpm for 5 min. Next, the electrode was immersed and washed in ultrapure water, acetate buffer and ultrapure water again at OCP and 300 rpm for 1, 5 and 1 min, respectively. (4) The ORR performance, background and stripping CV of the poisoned electrode were measured following the same procedure described in step (2). Subsequently the last step (4) was repeated to verify that the catalyst was recovered after the stripping.

2.5. Demonstration in a fuel-cell environment

The characterization of Im-FeNC concludes with a proof-of-concept study that confirms the catalyst can enable the ORR in MEA configuration, in an actual PEMFC system, and to evaluate its performance. The MEA-fabrication procedure begins with the growth of a catalytic deposit on top of gas-diffusion layer (GDL), done via drop-casting method. For this, inks were prepared by solving a certain amount of Im-FeNC in ethanol (98% absolute from Sigma Aldrich). Nafion 1100 EW solution (5 wt% in lower aliphatic alcohol and water, Sigma-Aldrich) was added, according to an ionomer/catalyst weight ratio of 2/3 (40/60 wt%). The inks were sonicated in an ultrasound bath at room temperature for at least 1 h and, using precision syringes, casted on carbon-based GDLs (Sigracet® 22 BB). The GDLs were fixed on the surface of a hotplate at 90 °C during the deposition process. The MEAs were assembled by sandwiching a proton-exchange membrane (Nafion® 211) in between an Im-FeNC-coated GDL (cathode) and a commercial electrode consisting in a GDL (Sigracet® 29 BC) covered with Pt/C 40 wt% catalyst (anode). Finally, the MEAs were pressed between flat graphite plates by tightening the clamping screws at a torque of 3 N m and heated at 90 °C for 15 min.

Once assembled, MEAs were tested in a single-cell commercial hardware with a mixed-serpentine multichannel flow-field, made in graphite, of an active area of 1 cm^2, and compatible with the differential-cell configuration. The test stand employed in this study was developed in-house at the German Aerospace Center (DLR), equipped with programmable logic controllers and a commercial electronic load (from H&H, model ZS506-4NV). The gas mass flow rates were regulated at the cell inlets whereas the pressure was controlled at the cell outlets. For humidifying the gases, water evaporators from Bronkhorst High-Tech B. V. were used, and gas lines connecting the humidifiers to the cell were heated up to avoid condensation. All the experiments were done under H$_2$/air operation, fixing the relative humidity (RH) at 100%, the pressure at 300 kPa$_{abs}$, and the cell temperature at 80 °C. To avoid fuel starvation phenomena and preserve homogeneity, the gas flow was set constant at high-stoichiometry values.

3. Results and discussion

3.1. Physicochemical characterization

As depicted in Scheme 1, the polymerization of melamine and terephthalaldehyde in the presence of Zn(NO$_3$)$_2$ and Fe(NO$_3$)$_3$ resulted in an amorphous material as deduced from the absence of diffraction peaks in the x-ray diffractogram, data not shown. The diffractograms of the catalysts obtained after the thermal treatments, namely Im-FeNC-1HT and Im-FeNC-2HT, are shown in Fig. S1a in the Supporting Information. The XRD patterns exhibit broad peaks at ca. 25° and ca. 44° corresponding to the (002) and (101) planes of graphitic carbon. In addition, a weak peak at 44° can be observed for Im-FeNC-1HT, which can be ascribed to metallic Fe, Fe$_3$C and/or Fe$_x$N phases [35,36]. The intensity of this peak decreases significantly after the acid leaching and second thermal treatment, evincing the removal of Fe particles. A careful inspection of Fig. S1a reveals the presence of a very weak peak in the diffraction pattern of Im-FeNC-2HT around 80° which, in line with previous reports, can indicate the presence of a small fraction of iron particles (metallic iron and/or iron carbide) wrapped within several graphite layers remains in the catalyst after the acid leaching process [36]. The presence of such particles is confirmed from the TEM micrographs shown in Fig. S2. Raman spectra of the catalysts are shown in Fig. S3. The presence of two peaks at ca. 1340 and 1608 cm^{-1}, usually identified as the D and G bands, respectively, indicates the generation of a graphitic material after the thermal treatments. Note that the Raman spectrum of the material obtained after the wet polymerization of the precursors previous to the thermal treatment. Finally, a moderate increase of the relative intensity of the G/D bands from 1.9 to 2.1, is observed after the second thermal treatment.

The specific surface area of the Im-FeNC-2HT was evaluated from the N$_2$ adsorption-desorption isotherm. The catalyst showed a Type I(b) isotherm with a small H4 hysteresis loop, see Fig. S1b. This type of isotherm is common for microporous catalysts, which exhibit a quick uptake at low p/p^0 due to improved adsorption in micropores. On the other hand, the hysteresis loop can be ascribed to its micro-mesoporosity, similar to previously reported Fe/N/C catalysts [16]. The BET surface area of Im-FeNC-2HT is 650 m^2 g^{-1} of which 370 m^2 g^{-1} and 280 m^2 g^{-1} correspond to micropore and external surface area, respectively.

It is well documented, that the catalysts obtained from the thermal treatment of iron/nitrogen/carbon precursors, such as the one reported in this work, present a small fraction of iron particles, along with atomically dispersed iron atoms coordinated to several N atoms in a graphitic carbon matrix. As shown above, XRD and TEM analysis identified the presence of iron particles, whereas the formation of a graphitic matrix was deduced from the Raman spectra. The identification of the presence and structure (coordination environment, oxidation state and abundance) of the atomically dispersed iron atoms is more difficult, and to date the most reliable approach to actually identify the nature of such isolated iron atoms is ^{57}Fe Mössbauer spectroscopy. As shown in Fig. 1a, the room temperature Mössbauer spectrum for Im-FeNC-2HT is rather complex. It is dominated by intense, broad, paramagnetic signals in the center of the spectrum and some minor magnetic components. The spectrum resembles some of the spectra reported in the recent literature for atomically dispersed iron atoms in Fe/N/C like catalysts [12], and was fitted and interpreted using the species, and their corresponding assignments, given in such references. Fig. 1b shows a Mössbauer spectrum recorded a room temperature in a lower range of velocities to determine with better accuracy the hyperfine parameters of the various species. A low temperature spectrum, 8.5 K, was also recorded (Fig. 1c) to determine whether the doublets observed in the room temperature spectra contain contributions from superparamagnetic iron oxides.

Our fit model considered one singlet, four doublets and three magnetic sextets. The hyperfine parameters and relative areas obtained from the fit of the room temperature data, together with their assignment to different chemical species, are shown in Table S1 of the Supporting Information.

The most intense contribution, accounting for ca. 42% of the spectral area, corresponds to doublet D1 which has been recently associated with a high-spin O$_2$–Fe(III)N$_4$/C species in a FeN$_4$C$_{12}$ environment [12]. This doublet, having the same quadrupole splitting and a larger isomer shift (this increase resulting from the second-order Doppler shift), is also present in the 8.5 K spectrum confirming the Fe(III) high-spin character of this species since no temperature variation is expected for the quadrupole splitting in this case. The second most intense paramagnetic doublet (10% of the spectral area) corresponds to doublet D2 which has been attributed to a low-spin Fe(II)N$_4$ species in a FeN$_4$C$_{10}$ configuration [12]. Similarly, to doublet D1, the quadrupole splitting of D2 does not increase with decreasing temperature, confirming its low-spin Fe(II) nature. The spectrum also contains two minor paramagnetic doublets with hyperfine parameters characteristic of doublets D3 y D5 [37], see
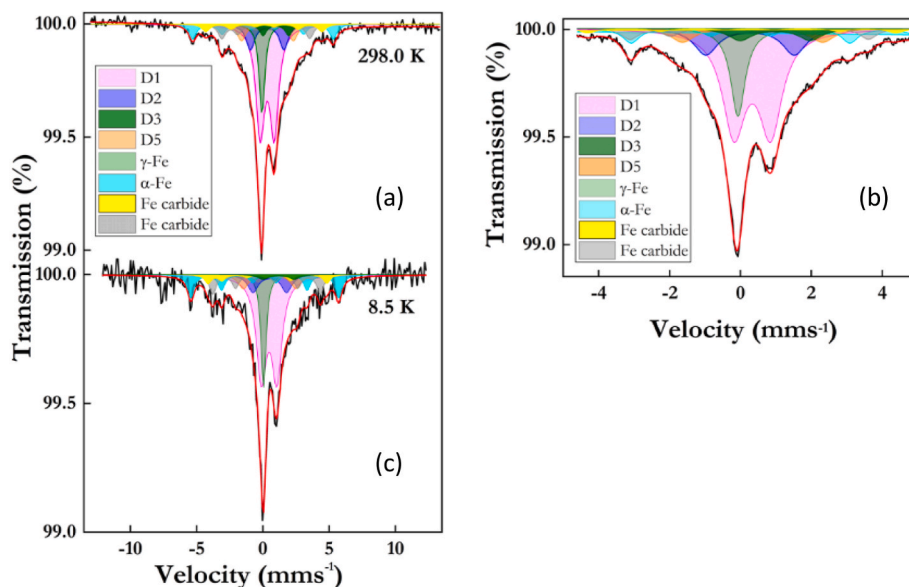
Fig. 1. (a) Room temperature ^{57}Fe Mössbauer spectrum recorded from Im-FeNC-2HT; (b) Room temperature Mössbauer spectrum recorded in a narrower range of velocities; (c) Mössbauer spectrum recorded at 8.5 K.

Table S1.

The intense singlet observed in the room temperature spectrum has been associated with superparamagnetic α-Fe [37]. However, the singlet is also observed in the 8.5 K spectrum instead of the characteristic sextet that should be expected if the room temperature singlet was due to α-Fe. The occurrence of a singlet instead of a sextet at such lower temperature would imply an extremely small particle size as to remain paramagnetic at 8.5 K, something that appears to be unlikely. In our view, this singlet is more likely associated with the presence of γ-Fe since this compound, despite being antiferromagnetically ordered below 77 K, shows a broadened singlet at low temperatures and has been observed in other

iron-carbon systems [38,39].

The room temperature Mössbauer spectrum also contains three magnetic sextets: a main one characteristic of α-Fe and two other minor ones associated to iron carbides having different stoichiometries. Finally, the 8.5 K spectrum does not show any magnetic sextet which could be associated to iron oxides, confirming that the sample does not contain any superparamagnetic iron oxide species. The observation of these species is consistent with the, XRD and TEM analyses shown in the supporting information, that reveal the presence of a small fraction of iron particles in both Im-FeNC-1HT and Im-FeNC-2HT, particularly in the former sample. The Fe 2p core-level (Fig. S4) spectrum of Im-FeNC-
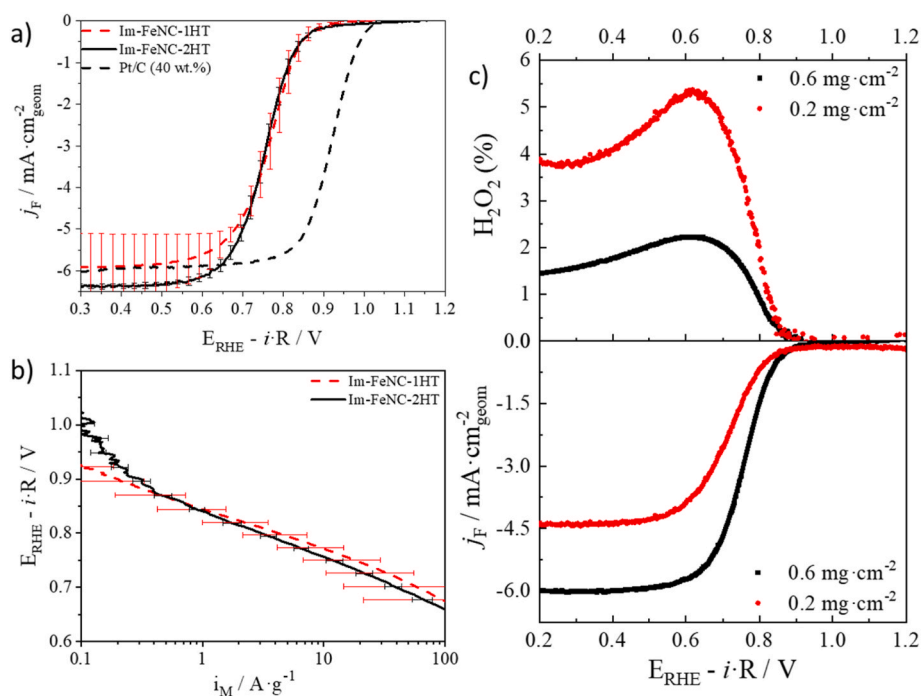

Fig. 2. a) ORR polarization curves recorded at 10 mV s^{-1} and 1600 rpm in O$_2$-saturated 0.1 M HClO$_4$ (0.6 mg$_{cat}$·cm^{-2}). Error bars were obtained by recording at least 3 measurements from different batches; b) mass-specific normalized ORR activities; c) RRDE measurement of Im-FeNC-2HT at two different loadings: % H$_2$O$_2$ released into the electrolyte (0.1 M HClO$_4$) with its corresponding ORR polarization curves recorded at 10 mV s^{-1} and 1600 rpm.

2HT shows two doublets with the Fe $2p_{3/2}$ core levels at ca. 709.5 and 711.9 eV, ascribed to iron oxidized species, typically Fe (II) and Fe (III), with the former peak being ca 2 times more intense than the latter. The precise nature of the iron species cannot be determined only by the binding energy of the XPS peaks. However, the absence, or small intensity, of the satellite peaks suggest that presence of Fe (II) species in low spin configuration, in good agreement with the Mössbauer analyses.

3.2. Assessment of catalytic performance

The background current density recorded in Ar-saturated electrolyte for Im-FeNC-1HT and Im-FeNC-2HT, which are related to the capacitive current, can be seen in Fig. S5. The backgrounds were rectangular shaped, as it is usually observed for carbonaceous materials [8,40]. The ORR polarization curves obtained in O_2-saturated 0.1 M $HClO_4$ (background and solution resistance corrected) are shown in Fig. 2 along the activity measured for Pt/C. Both Im-FeNC catalysts show similar ORR activity, regardless of the thermal treatment, even though the activity is still far from that obtained with a commercial Pt/C catalyst. In Table 1 representative activity parameters for the ORR activity are collected. E_{onset}, defined as the potential at which a current of 0.1 mA cm^{-2} is reached, was 0.90 and 0.93 V for Im-FeNC-1HT and Im-FeNC-2HT, respectively. Similarly, the half-wave potential, $E_{1/2}$, difference between the values for Im-FeNC-1HT (0.77 V) and 2HT (0.76 V) is negligible. As expected, more positive potentials were recorded for Pt/C (E_{onset} = 1.02 V and $E_{1/2}$ = 0.92 V). Since the $E_{1/2}$ values are similar for both homemade Fe/N/C catalysts, it can be assumed that the mixed and diffusional controlled regions are not much affected by the acid leaching and second pyrolysis step. Similarly, it seems that those steps do not have a slight impact on the active sites responsible for the ORR at low overpotential, indicating that the active sites for the ORR in acid are not affected by the acid leaching process. However, as observed in Fig. 2a, the error bars for the catalyst subjected to only one thermal treatment (Im-FeNC-1HT) are larger than the ones of the catalyst subjected to acid leaching and a second thermal treatment (Im-FeNC-2HT), especially within the diffusion limiting region. As shown below, comparable H_2O_2 productions were obtained for both catalysts, so we ascribe the larger error bars recorded with Im-FeNC-1HT to a less homogeneous deposition of Im-FeNC-1HT on the RDE electrode, suggesting that the catalyst resulting after acid leaching and the second thermal treatment is dispersed more easily on the electrode.

To compare the ORR activity of Fe/N/C catalysts mass activities are used. They are calculated from the kinetic currents obtained from mass-transport-corrected Faradaic currents using the Koutecky-Levich (K-L) equation:

$$i_K = \frac{(-i_f \times i_{lim})}{i_f - i_{lim}} \tag{Eq. 2}$$

where i_K is the kinetic current, which is negative for reduction reactions, and i_{lim} is the limiting current. The ORR mass activity is determined by the following formula:

$$i_m = \frac{i_k}{m_{cat}} \tag{Eq. 3}$$

where i_m is the mass activity and m_{cat} is the catalyst loading.

The mass activities of both catalysts are depicted in Fig. 2b, with i_m values at 0.8 V collected in Table 1. It shall be noted that i_m values are in the same order of magnitude, 4.2 and 3.4 A g^{-1} for Im-FeNC-1HT and for Im-FeNC-2HT. Concerning the Tafel slopes, values of 74 and 83 mV dec^{-1} for Im-FeNC-1HT and Im-FeNC-2HT were estimated, pointing out that slightly different overpotentials are required to produce high currents. Hence, it can be asserted that imine-based polymers are an effective precursor to create high-performance Fe/N/C catalysts, displaying ORR activities in line with the best Fe–N–C catalysts obtained without using 2-methylimidazole (or ZIF-8) precursors, see Table S2.

The ORR is a multi-electron process that can proceed through a 4 e^- process or via a $2 + 2$ e^- pathway. When the serial pathway takes place, H_2O_2 is produced as an intermediate that can be further reduced to produce water. However, this pathway is undesired since hydrogen peroxide can lead to oxidation or degradation of the carbon structure in the catalysts, involving the detachment of active sites causing a performance drop.

In order to determine contribution of each pathway was assessed by performing RRDE experiments to quantify the production of H_2O_2 over the ORR.

The polarization curves of RRDE experiments and the amount of hydrogen peroxide generated with two different catalyst loadings of Im-FeNC-2HT are shown in Fig. 2c. When a catalyst loading of 0.6 g cm^{-2} was used the amount of H_2O_2 detected was lower than that obtained with 0.2 g cm^{-2} (~2% compared to 5.5% at 0.6 V, which is the potential at which the maximum hydrogen peroxide formation is observed). The number of electrons exchanged in the overall reaction is estimated using the equation:

$$n^o \, e^- = 4 - \frac{\% \, H_2O_2}{50 \, \%} \tag{Eq. 4}$$

The number of electrons transferred during the ORR at 0.6 V with catalyst loadings of 0.6 and 0.2 g cm^{-2} are ~3.96 e^- and ~3.89 e^-, respectively. Therefore, it was confirmed that using this catalyst the ORR proceeds via a direct pathway, which is the desired one. However, the low H_2O_2 generation detected in this study could be associated to a loading effect, which can lead to a dummy 4-electron estimation instead of a $2 + 2$ electron pathway [16,31]. Given that only a slight increase in the number of exchanged electrons was observed for lower catalyst loadings, it can be concluded that the 4-electron pathway determined for this catalyst is not an artefact due to catalyst loading. As shown Fig. S7, a similar profile of H_2O_2 production is similar for both Im-FeNC-1HT and Im-FeNC-2HT, including similar error bars.

To test the durability and stability of Im-FeNC-2HT the accelerated stress test (following DOE's protocol) described in section 2 was applied. In Fig. 3 the ORR activity was depicted after different cycles in Ar- and O_2-saturated electrolytes at 1600 rpm and using 0.6 g cm^{-2} as catalyst loading. The ORR polarization curves collected after 10k cycles, in the Ar-saturated electrolyte, indicate that the ORR activity remains similar at 0.8 V to the initial activity. However, a slight decrease of the limiting current could be observed. After a 20k cycles a 27% loss of normalized mass activity was observed at 0.8 V vs RHE. On the other hand, when the AST was carried out in O_2-saturated electrolyte the activity dropped much faster even though the polarization curve recorded after 1000 cycles was close to the initial ORR curve. Performance drops of 55% and

Table 1
Parameters of interest extracted from ORR curves and mass activities results.

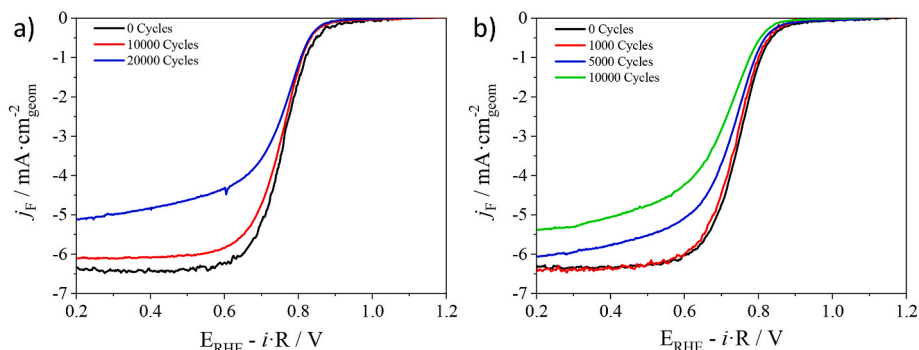|	E_{onset} (V) at −0.1 mA cm^{-2}	$E_{1/2}$ (V)	j_k (mA·cm^{-2}) @ 0.8 V	i_m (A·g^{-1}) @ 0.8 V	Tafel slope (mV·dec^{-1})
Im-FeNC-1HT (0.1 M $HClO_4$)	0.90	0.77	1.6	4.2	74
Im-FeNC-2HT (0.1 M $HClO_4$)	0.93	0.76	1.5	3.4	83
Im-FeNC-1HT (0.5 M acetate buffer)	0.98	0.84	24.0	37.1	67
Im-FeNC-2HT (0.5 M acetate buffer)	0.95	0.83	15.3	22.4	69

Fig. 3. ORR polarization curves (10 mV s^{-1} and 1600 rpm) for Im-FeNC-2HT at BoE and after 10k and 20k load cycles recorded in a) in Ar-saturated 0.1 M HClO$_4$ and b) in O$_2$-saturated 0.1 M HClO$_4$.

56% were detected after 5k and 10k cycles at 0.8 V. Moreover, the decrease in the limiting current was previously ascribed to a loss of active sites over the cycles in 0.1 M HClO$_4$ [8,19]. This is proof of the formation of durable active sites with a similar performance and comparable to the best reported ones [41,42].

The evolution of the N-containing species after the ASTs in O$_2$- and in N$_2$- saturated electrolytes was studied by XPS using synchrotron radiation. First, the N 1s core-level spectrum of Fe-imine-2HT-BoL (BoL, beginning of life) was recorded. Following previous literature, the N 1s region was deconvoluted into 5 peaks, corresponding to pyridinic-N, Fe-N$_x$, pyrrolic-N, N-graphitic and nitrogen oxides at ca. 398.6, 399.9, 400.9, 401.8 and 403–405 eV, [43–46]. XPS spectra of the catalysts recovered after the AST in N$_2$- (Fe-imine-2HT-EoL-N$_2$) and in O$_2$- (Fe-imine-2HT-EoL-O$_2$) saturated electrolytes were also collected. The spectra are shown in Fig. 4. As observed, pyrrolic-N is the main species in Fe-imine-2HT-BoL, followed by pyridinic-N and Fe-N$_x$. After the ASTs, the intensity of the overall N 1s core-level region decreases suggesting the loss of the N-containing moieties during the ORR. A careful inspection of the spectra in Fig. 4 reveals that pyrrolic-N species decreases to a greater extent than those of pyridinic-N and Fe-N$_x$, suggesting that pyrrolic-N, especially during the AST in the O$_2$-saturated electrolyte, are less stable during ORR than pyridinic-N species. This finding is in line with previous reports that indicate that pyridinic-N or FeN$_4$C$_{10}$-like ensembles, identified by the D2 doublets in the Fe Mössbauer spectra, are responsible for the long-term ORR activity of Fe/N/C like catalysts in acid electrolyte. On the other hand, FeN$_4$C$_{12}$ ensembles (D1 doublet) display higher initial ORR activity but lack stability [13,22].

Lastly, in order to deepen into the understanding of the kinetic activity some kinetic metrics, such as the active metal site density (SD$_{mass}$) and the catalytic turnover frequency (TOF), were estimated and compared to those previously reported for state-of-the-art Fe/N/C catalysts.

Electrochemical stripping of NO was performed to determine the number of accessible sites. In the estimate it was assumed that one adsorbed NO is reduced per site and that NO stripping followed a three-electron reduction to produce hydroxylamine [11]:

$$NO - Fe(III) - N_4 + 3e^- + 3H^+ \rightarrow Fe(III) - N_4 + NH_2OH \quad (1)$$
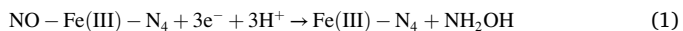
The number of accessible sites per gram of catalyst (site density, SD$_{mass}$) was estimated from the electric charge necessary to reduce NO adsorbed onto Fe. The following equation was used to calculate the site density [34]:

$$SD_{mass}\left(sites \cdot g^{-1}\right) = \frac{Q[A \cdot V \cdot cm^{-2}] \cdot N_A\left[Atom \cdot mol^{-1}\right]}{n \cdot w\ [V \cdot s^{-1}] \cdot F[A \cdot s \cdot mol^{-1}] \cdot L[g \cdot cm^{-2}]} \quad (Eq.\ 5)$$

Where Q is the charge associated to NO reduction (grey area in Supplementary Figs. S7d and S8d for Im-FeNC-1HT and -2HT, respectively), n is the number of electrons involved in the NO reduction (3 in this
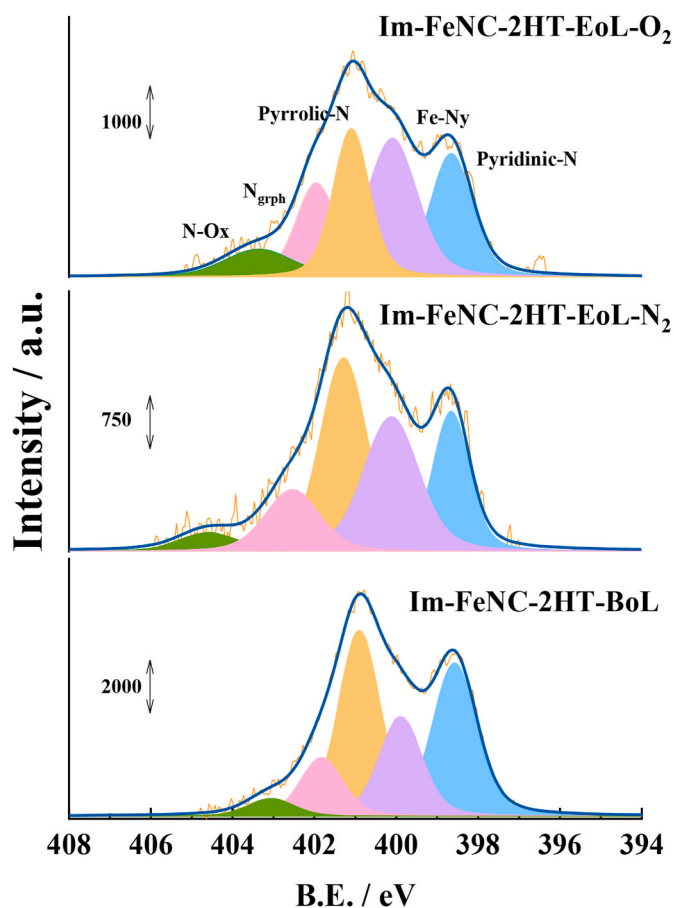

Fig. 4. N 1s core-level spectra for Im-FeNC-2HT-BoL (bottom panel), Im-FeNC-2HT-EoL-N$_2$ (central panel) and Im-FeNC-2HT-O$_2$ (upper panel). Peaks for pyrrolic-N (blue), Fe$_x$N (purple), pyrrolic-N (ochre), graphitic-N (magenta) and N-oxides (green) are observed. (For interpretation of the references to colour in this figure legend, the reader is referred to the Web version of this article.)

study); N$_A$ is the Avogadro's constant, F is the Faraday's constant, ω is the scan rate and L is the catalyst loading. The area is calculated from the difference between the current density obtained deducting the first voltammogram of the background scan to that recorded with the poisoned electrode between 0.4 V and −0.3 V vs RHE (Figs. S7c and S8c). The value of SD$_{mass}$ estimated by stripping of NO generated from NO$_2^-$ for the Im-FeNC-1HT and Im-FeNC-2HT catalysts were 4.6·10^{19} and 4.4·10^{19} sites·g^{-1}. As observed, the second heat treatment does not modify the site density of the catalysts. To put this value into context, a SD$_{mass}$ of 4.6·10^{19} sites$_{Fe}$·g$_{cat}^{-1}$ translates into ca. 0.4 wt% Fe in the

catalyst. A Fe/C surface atomic ratio of 0.0043 has been obtained by XPS. This value corresponds to a (surface) Fe loading of ca. 2 wt% (assuming carbon as the other only component). In order to compare the SD_{mass} obtained for the studied catalysts with other catalysts, it should be taken into account that most SD_{mass} values reported in the literature were calculated by assuming a 5-electron reduction of NO [32]. We have recalculated the values reported in the literature by assuming a 3-electron reduction of NO. The SD_{mass} values thus obtained are collected in Table 2. Im-FeNC-1HT and -2HT both exhibited a high amount of active sites, only exceeded by FeNC-CVD-750 [11], a ZIF-derived catalyst obtained by chemical vapour deposition, which records the highest SD_{mass} reported to date.

The ORR polarization curves measured in the O_2-saturated 0.5 M acetate buffer for Im-FeNC-1HT and Im-FeNC-2HT are shown in Figs. S7a and S8a, respectively. As observed, both catalysts display high ORR activity at such conditions. In both cases, the ORR activity dropped significantly after NO_2^- poisoning, in good agreement with previous reports [32,34]. After NO stripping the catalysts recovered their initial ORR activity. Thus, it was corroborated that adsorbed NO are the main responsible for the loss of the ORR performance detected. Since the activity did not drop completely after poisoning, due to the fact that not all of the active sites were blocked, the TOF was estimated by quantifying the difference in the mass kinetic current (i_{mass}) between the unpoisoned and poisoned catalyst at a certain potential (0.8 and 0.85 V vs. RHE in this work). The Tafel plots and i_{mass} values are shown in Figs. S7b and S8b. The TOF was determined according to the following equation [34]:

$$TOF \left(electron \cdot site^{-1} \cdot s^{-1}\right) = \frac{\Delta i_{mass}[A \cdot g^{-1}] \cdot N_A [Atom \cdot mol^{-1}]}{SD_{mass}[sites \cdot g^{-1}] \cdot F[A \cdot s \cdot mol^{-1}]} \quad \text{(Eq. 6)}$$

The TOF values estimated for the catalysts studied here and for other benchmarking catalysts, recalculated assuming a three-electron reduction for the NO stripping, are gathered in Table 2. The TOF (0.8 V vs. RHE) values obtained for Im-FeNC-1HT and Im-FeNC-2HT are 4.2 and 4.9 electron·site^{-1}·s^{-1}. Hence, even though the second thermal treatment does not increase the site density it does seem to increase their yield. These TOF values are relatively high compared to those reported previously, which are usually below 4 electron·site^{-1}·s^{-1} [32,34]. PAJ, synthesized via hard templating with fumed silica, is the catalyst whose TOF (4.34 electron·site^{-1}·s^{-1}) is the closest to that of Im-FeNC-2HT [34]. In fact, the TOF estimated at 0.85 V vs RHE (0.6 electron·site^{-1}·s^{-1}) for Im-FeNC-2HT is higher than the TOF reported by Jiao et al. [11] for FeNC-CVD-750 at 0.85 V vs RHE (0.47 electron·site^{-1}·s^{-1}). Note that the TOF values reported above have been determined from i_{mass} activities recorded in acetate buffer (pH 5.2)

Table 2
Kinetic metrics, mass-site densities (SD_{mass}) and the turnover frequencies (TOF), calculated at 0.80 and 0.85 V_{RHE} for the catalysts studied in this work and for state-of-the-art catalysts measured under the same reaction conditions. All of the TOF values reported in this table were obtained from the mass-specific ORR activities recorded in acetate buffer electrolyte (pH ca. 5.2). To estimate the SD_{mass} it was assumed that NO stripping entailed a three-electron reduction.

	SD_{mass} (sites·g^{-1})	TOF (electron site^{-1}·s^{-1})	Reference
Im-FeNC-1HT	4.61·10^{19}	4.20	This study
Im-FeNC-2HT	4.40·10^{19}	4.88	This study
CNRS	2.40·10^{19}	0.39	[47,48]
ICL	1.43·10^{19}	0.58	[33]
PAJ	0.42·10^{19}	4.34	[34]
UNM	1.05·10^{19}	2.07	[34]
FPHEN3	0.71·10^{19}	4.00	[16]
FBPY1	0.37·10^{19}	1.90	[16]
FeNC-CVD-750 at 0.85 V_{RHE}	10.0·10^{19}	0.47	[11]
Im-FeNC-2HT at 0.85 V_{RHE}	4.40·10^{19}	0.60	This study

electrolytes.

In order to benchmark the ORR activity of the catalysts reported in this work with the state-of-the-art catalysts in the literature, a site density–ORR turnover frequency map (SD_{mass}–TOF ORR reactivity map) was plotted [34,49], see Fig. 5. Each catalyst falls on a hyperbolic iso-mass activity curve, i_m allowing to assess the effect of synthesis parameters on the catalytic activity and different strategies can be designed. From the map it can be inferred that, while catalyst activity can be improved by either increasing the SD_{mass} or the TOF, focusing on the enhance of the site density is a better strategy since iso-mass activity curves are closer to each other [34]. Previously reported catalysts are found either at the low-SD_{mass} region (bottom-side of the graph) or at the low-TOF region (left-side of the graph), as they fail to achieve high values on both properties at the same time, and leading to relatively low mass currents < 4 A g^{-1} at 0.8 V vs RHE. On the contrary, Im-FeNC-2HT features both a considerably high SD_{mass} and a relatively high TOF, falling around the middle position (elbow) of the iso-mass curves and reaching almost 35 A g^{-1} at 0.8 V vs RHE. Nevertheless, the kinetic metrics at higher voltages (0.85 V vs RHE) of Im-FeNC-2HT (4 A g^{-1}) are yet lower than those of FeNC-CVD-750 (7 A g^{-1}), indicating room for improvement of Im-FeNC-2HT by increasing the SD_{mass} (which can also be derived from its position in the map, slightly below the bisector of the first quadrant).

The results reported in Fig. 5 have been obtained at pH = 5.2. It is known that the kinetics for ORR with Fe–N–C like catalysts is strongly dependent on the pH scale, displaying higher kinetics at high pH values. Thus, the ORR activity of a thermally treated Fe–N–C catalyst at high potentials is the same in the pH range between 0 and 9, increasing at higher pH values [32]. However, this not the case for the catalysts studied in this work. As observed in Table 1, the pure kinetic currents (j_{kin}) and the mass-specific activity (i_{mass}) obtained in the buffer acetate electrolyte (pH = 5.2) are higher than those obtained in the RDE experiments conducted in 0.1 M HClO$_4$. Therefore, we have also calculated TOF of the Im-FeNC-2HT from the activity data recorded in 0.1 M HClO$_4$. For that, we first determined the site density of Im-FeNC-2HT from *ex situ* CO cryo-chemisorption $SD_{mass,CO}$ (see Fig. S9). We obtained a $SD_{mass,CO}$ of 10·10^{19} sites·g^{-1}, a value that, despite the different nature of the analyses, correlates well with the SD_{mass} value obtained
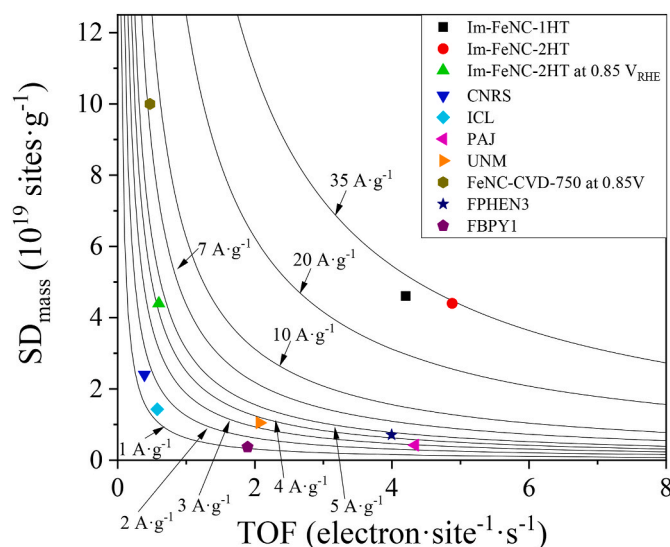
Fig. 5. SD_{mass}–TOF ORR reactivity maps for the Im-FeNC catalysts reported in this work at 0.80 V_{RHE} and at 0.85 V_{RHE}. SD_{mass}-TOF values for state-of-the-art catalysts (CNRS, ICL, PAJ and UNM [34], FPHEN3 and FBPY1 [16], FeNC-CVD-750 [11]) are reported for comparison. Mass-specific ORR activities used to calculate TOF values of all catalysts were obtained at pH = 5.2. SD_{mass} values reported in this figure have been obtained from in-situ NO stripping (see experimental section).

from nitrite reduction. The CO-derived TOF (TOF_{CO}) obtained for Im-FeNC-2HT (using the i_{mass} activity recorded in the 0.1 M $HClO_4$ electrolyte) is 0.22 electron·site^{-1}·s^{-1}. This value is lower than the one obtained in the acetate electrolyte, ca. 4.8 electron·site^{-1}·s^{-1} (see Fig. 5). This trend, *i.e.*, smaller TOF values obtained from $SD_{mass,CO}$ and i_{mass} at low pH of ca. 1 and lower, has been also reported by Primbs et al. for state-of-the-art pyrolyzed Fe–N–C catalysts in 0.5 M H_2SO_4 [34]. Note, nonetheless, that the TOF_{CO} value for Im-FeNC-2HT are lower, yet in the same order of magnitude, that the TOF_{CO} values reported for state-of-the-art catalysts measured in 0.5 M H_2SO_4, see Fig. 6.

3.3. Single-cell proof-of-concept

The testing in MEA configuration was restricted to the fully treated catalyst, Im-FeNC-2HT, as it exhibits a larger TOF value, being expected to display a higher ORR activity also in a PEMFC environment. Tests were carried out in potentiostatic mode and under the conditions described in section 2.5. A MEA with a catalyst load of 3.5 mg cm^{-2} of Im-FeNC-2HT at the cathode was enclosed and clamped in the cell hardware by gradually tightening the screws up to a torque of 3 N m. At the beginning of the test, the MEA subjected to a load procedure consisting of voltage-cycling periods and steady-state operation for 2 h. The polarization curve measured after activation can be seen in Fig. 7 (data presented without iR-correction).

The maximum power density value of 170 mW cm^{-2} shown by Im-FeNC-2HT in this study is superior to those shown by Fe/C/N catalysts obtained from melamine-based precursors [8,25,26]. Nevertheless, this performance remains low when compared with some of the latest Fe/C/N catalyst developed in the state of the art [3,5], mainly those derived from ZIF-8 precursors [11,17,18,37,48]. However, a straightforward comparison is often not possible due the large number of experimental parameters involved in single-cell testing, leading to a diverse zoology of characterization conditions in the literature. For instance, several of the referred studies use significantly larger catalyst loadings, though lower pressures, as well as employing pure O_2 as an oxidant instead of air. In addition, recent studies have discussed the strong effect that the ink composition can have on the performance of Fe/C/N catalyst, highlighting the importance of a detailed optimization
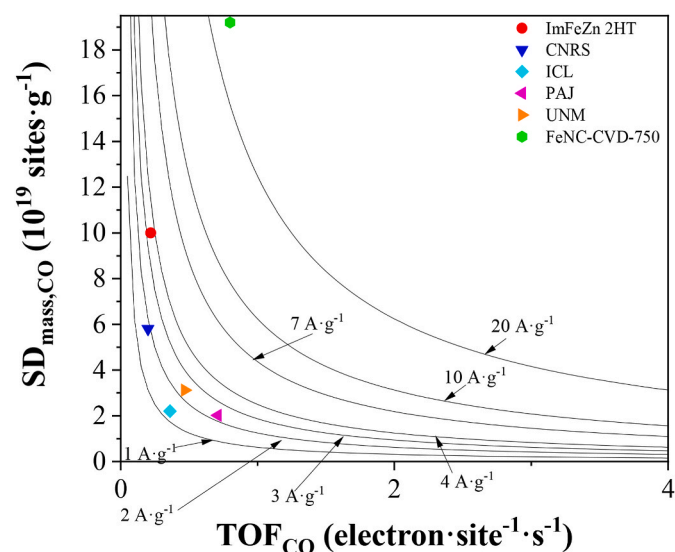

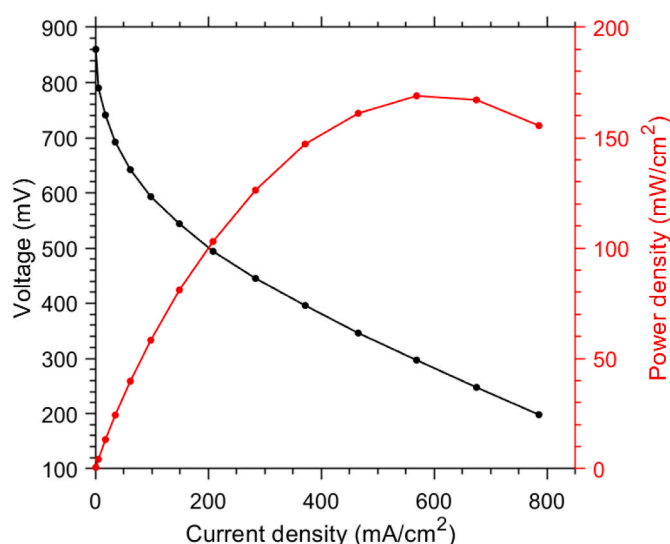**Fig. 7.** Fuel-cell polarization curve (black dots) and the corresponding power density (red dots) measured with H_2/air flow rates of 300 sccm at 80 °C, 100% RH and 300 kPa, for catalyst loadings of 3.5 mg cm^{-2} of Im-FeNC-2HT at the cathode and 0.3 mg cm^{-2} of Pt/C 40 wt% at the anode. (For interpretation of the references to colour in this figure legend, the reader is referred to the Web version of this article.)

of the ink parameters [4]. Such differences in the testing procedures and ink composition, along with the relative low BET specific surface area of Im-FeNC-2HT (ca. 650 m^2 g^{-1} *vs* ca. 1100 m^2 g^{-1} of the state-of-the-art ZIF-8 based catalysts) may explain the moderate in-MEA performance obtained for the Im-FeNC catalyst despite their relatively large SD_{mass} and TOF values recorded in RDE configuration. Still, the present results confirm that Im-FeNC-2HT promotes the ORR in MEA configuration, being possible to use it in a PEMFC under relevant conditions.

4. Conclusions

A novel Fe/N/C catalyst, Im-FeNC, with a high nitrogen/carbon ratio was synthesized via the wet-polymerization of an imine-based framework. The polymer was later subjected to thermal treatments and acid leaching. It was observed that Fe particles were efficiently removed after acid leaching and the second pyrolysis. Furthermore, after the second heat treatment a further enhancement of the ORR activity is observed. Studies conducted in RRDE configuration showed that the catalysts obtained promoted the four-electron pathway to reduce O_2 producing H_2O. The catalyst was more stable in Ar-saturated electrolyte in comparison to O_2-saturated electrolyte. Nevertheless, the catalyst activity only decreases significantly after 20k and 10k cycles in Ar- and O_2-saturated electrolyte, respectively. Both Im-FeNC catalysts exhibited a high amount of active sites, with a SD_{mass} around 4.4·10^{19} sites·g^{-1}. Moreover, the catalyst displays high intrinsic ORR activity, with a TOF value for Im-FeNC-2HT of 5.28 electron·site^{-1}·s^{-1}. In view of these results, namely high SD_{mass} and TOF, it can be concluded that imine-based frameworks are suitable precursors to synthesize efficient Fe/N/C catalysts for the ORR in acid electrolyte. Additionally, a concept-validation test was carried out in a PEMFC, demonstrating its feasibility for triggering the ORR also in MEA configuration.

CRediT authorship contribution statement

ATM, AG, DL synthesized the catalysts and conducted RDE experiments. JM conducted Mössbauer experiments. LP conducted TEM analyses. ATM, AG, DL, MS and MR conducted catalyst characterizations. PF, DG and GH conducted XPS synchrotron experiments. AGC, JT, DGS and AF produced MEAs and conducted PEMFC experiments. MR and SR

Fig. 6. Site density–ORR turnover frequency maps ($SD_{mass,CO}$–TOF_{CO} ORR reactivity maps) for Im-FeNC-2HT at 0.80 V_{RHE} and for state-of-the-art catalysts (CNRS, ICL, PAJ and UNM [34], FeNC-CVD-750 [11]). TOF_{CO} values were determined from RDE measurements in 0.5 M H_2SO_4 (CNRS, ICL, PAJ, UNM and FeNC-CVD-750) or 0.1 M $HClO_4$ (Im-FeNC-2HT). $SD_{mass,CO}$ determined from ex-situ CO cryo-chemisorption.

conceptualized and supervised the experiments. ATM, AGC and SR wrote the manuscript.

Declaration of competing interest

The authors declare that they have no known competing financial interests or personal relationships that could have appeared to influence the work reported in this paper.

Data availability

Data will be made available on request.

Acknowledgements

Appendix A. Supplementary data

Supplementary data to this article can be found online at https://doi.org/10.1016/j.jpowsour.2023.233223.

References

[1] Fuel Cells and Hydrogen Joint Undertaking (FCH), FCH, J. Undertaken, JU, IRENA, hydrogen roadmap europe. https://doi.org/10.2843/249013, 2019.

[2] H.A. Gasteiger, S.S. Kocha, B. Sompalli, F.T. Wagner, Activity benchmarks and requirements for Pt, Pt-alloy, and non-Pt oxygen reduction catalysts for PEMFCs, Appl. Catal., B 56 (2005) 9–35, https://doi.org/10.1016/j.apcatb.2004.06.021.

[3] L. Osmieri, J. Park, D.A. Cullen, P. Zelenay, D.J. Myers, K.C. Neyerlin, Status and challenges for the application of platinum group metal-free catalysts in proton-exchange membrane fuel cells, Curr. Opin. Electrochem. 25 (2021), 100627, https://doi.org/10.1016/j.coelec.2020.08.009.

[4] L. Osmieri, Q. Meyer, Recent advances in integrating platinum group metal-free catalysts in proton exchange membrane fuel cells, Curr. Opin. Electrochem. 31 (2022), 100847, https://doi.org/10.1016/J.COELEC.2021.100847.

[5] M. Shao, Q. Chang, J.-P. Dodelet, R. Chenitz, Recent advances in electrocatalysts for oxygen reduction reaction, Chem. Rev. 116 (2016) 3594–3657, https://doi.org/10.1021/acs.chemrev.5b00462.

[6] X. Deng, C. Huang, X. Pei, B. Hu, W. Zhou, Recent progresses and remaining issues on the ultrathin catalyst layer design strategy for high-performance proton exchange membrane fuel cell with further reduced Pt loadings: a review, Int. J. Hydrogen Energy 47 (2022) 1529–1542, https://doi.org/10.1016/J.IJHYDENE.2021.10.141.

[7] C. Domínguez, F.J. Pérez-Alonso, M. Abdel Salam, J.L. Gómez de la Fuente, S.A. Al-Thabaiti, S.N. Basahel, M.A. Peña, J.L.G. Fierro, S. Rojas, Effect of transition metal (M: Fe, Co or Mn) for the oxygen reduction reaction with non-precious metal catalysts in acid medium, Int. J. Hydrogen Energy 39 (2014) 5309–5318, https://doi.org/10.1016/j.ijhydene.2013.12.078.

[8] Á. García, M. Retuerto, C. Dominguez, L. Pascual, P. Ferrer, D. Gianolio, A. Serrano, P. Aßmann, D.G. Sanchez, M.A. Peña, S. Rojas, Fe doped porous triazine as efficient electrocatalysts for the oxygen reduction reaction in acid electrolyte, Appl. Catal. B Environ. 264 (2020) 118507, https://doi.org/10.1016/j.apcatb.2019.118507.

[9] J.-D.D. Yi, R. Xu, Q. Wu, T. Zhang, K.-T.T. Zang, J. Luo, Y.-L.L. Liang, Y.-B. Huang, R. Cao, Atomically dispersed iron–nitrogen active sites within porphyrinic triazine-based frameworks for oxygen reduction reaction in both alkaline and acidic media, ACS Energy Lett. 3 (2018) 883–889, https://doi.org/10.1021/acsenergylett.8b00245.

[10] A. Mehmood, M. Gong, F. Jaouen, A. Roy, A. Zitolo, A. Khan, M. Sougrati, M. Primbs, A.M. Bonastre, D. Fongalland, G. Drazic, P. Strasser, A. Kucernak, High loading of single atomic iron sites in Fe–NC oxygen reduction catalysts for proton

[11] L. Jiao, J. Li, L.L.R. Richard, Q. Sun, T. Stracensky, E. Liu, M.T. Sougrati, Z. Zhao, F. Yang, S. Zhong, H. Xu, S. Mukerjee, Y. Huang, D.A. Cullen, J.H. Park, M. Ferrandon, D.J. Myers, F. Jaouen, Q. Jia, Chemical vapour deposition of Fe–N–C oxygen reduction catalysts with full utilization of dense Fe–N4 sites, Nat. Mater. 20 (2021) 1385–1391, https://doi.org/10.1038/s41563-021-01030-2.

[12] T. Mineva, I. Matanovic, P. Atanassov, M.-T. Sougrati, L. Stievano, M. Clémancey, A. Kochem, J.-M. Latour, F. Jaouen, Understanding active sites in pyrolyzed Fe–N–C catalysts for fuel cell cathodes by bridging density functional theory calculations and 57 Fe mössbauer spectroscopy, ACS Catal. 9 (2019) 9359–9371, https://doi.org/10.1021/acscatal.9b02586.

[13] J. Li, M.T. Sougrati, A. Zitolo, J.M. Ablett, I.C. Oğuz, T. Mineva, I. Matanovic, P. Atanassov, Y. Huang, I. Zenyuk, A. Di Cicco, K. Kumar, L. Dubau, F. Maillard, G. Dražić, F. Jaouen, Identification of durable and non-durable FeNx sites in Fe–N–C materials for proton exchange membrane fuel cells, Nat. Catal. 4 (2021) 10–19, https://doi.org/10.1038/s41929-020-00545-2.

[14] K. Artyushkova, S. Rojas-Carbonell, C. Santoro, E. Weiler, A. Serov, R. Awais, R. R. Gokhale, P. Atanassov, Correlations between synthesis and performance of Fe-based PGM-free catalysts in acidic and alkaline media: evolution of surface chemistry and morphology, ACS Appl. Energy Mater. 2 (2019) 5406–5418, https://doi.org/10.1021/acsaem.9b00331.

[15] N.A. Besley, Density functional theory based methods for the calculation of X-ray spectroscopy, Acc. Chem. Res. (2020), https://doi.org/10.1021/acs.accounts.0c00171 acs.accounts.0c00171.

[16] M. Mazzucato, C. Durante, How determinant is the iron precursor ligand in Fe-N-C single-site formation and activity for oxygen reduction reaction? Electrochim. Acta 394 (2021), 139105 https://doi.org/10.1016/J.ELECTACTA.2021.139105.

[17] E. Proietti, F. Jaouen, M. Lefèvre, N. Larouche, J. Tian, J. Herranz, J.-P. Dodelet, Iron-based cathode catalyst with enhanced power density in polymer electrolyte membrane fuel cells, Nat. Commun. 2 (2011) 416, https://doi.org/10.1038/ncomms1427.

[18] S. Liu, C. Li, M.J. Zachman, Y. Zeng, H. Yu, B. Li, M. Wang, J. Braaten, J. Liu, H. M. Meyer, M. Lucero, A.J. Kropf, E.E. Alp, Q. Gong, Q. Shi, Z. Feng, H. Xu, G. Wang, D.J. Myers, J. Xie, D.A. Cullen, S. Litster, G. Wu, H.M.M. Iii, M. Lucero, A. J. Kropf, E.E. Alp, Q. Gong, Q. Shi, Z. Feng, H. Xu, G. Wang, D.J. Myers, J. Xie, D. A. Cullen, S. Litster, H.M. Meyer, M. Lucero, A.J. Kropf, E.E. Alp, Q. Gong, Q. Shi, Z. Feng, H. Xu, G. Wang, D.J. Myers, J. Xie, D.A. Cullen, S. Litster, G. Wu, Atomically dispersed iron sites with a nitrogen–carbon coating as highly active and durable oxygen reduction catalysts for fuel cells, Nat. Energy 7 (2022) 652–663, https://doi.org/10.1038/s41560-022-01062-1.

[19] Á. García, T. Haynes, M. Retuerto, P. Ferrer, L. Pascual, M.A. Peña, M. Abdel Salam, M. Mokhtar, D. Gianolio, S. Rojas, Effect of the thermal treatment of Fe/N/C catalysts for the oxygen reduction reaction synthesized by pyrolysis of covalent organic frameworks, Ind. Eng. Chem. Res. 60 (2021) 18759–18769, https://doi.org/10.1021/acs.iecr.1c02841.

[20] M. Liu, L. Guo, S. Jin, B. Tan, Covalent triazine frameworks: synthesis and applications, J. Mater. Chem. A 7 (2019) 5153–5172, https://doi.org/10.1039/C8TA12442F.

[21] K. Sakaushi, M. Antonietti, Carbon- and nitrogen-based organic frameworks, Acc. Chem. Res. 48 (2015) 1591–1600, https://doi.org/10.1021/acs.accounts.5b00010.

[22] Á. García, L. Pascual, P. Ferrer, D. Gianolio, G. Held, D.C. Grinter, M.A. Peña, M. Retuerto, S. Rojas, Study of the evolution of FeN C and Fe3C species in Fe/N/C catalysts during the oxygen reduction reaction in acid and alkaline electrolyte, J. Power Sources 490 (2021), 229487, https://doi.org/10.1016/j.jpowsour.2021.229487.

[23] L. Liu, C. Song, A. Kong, Nitrogen and sulfur-enriched porous bithiophene-melamine covalent organic polymers for effective capture of CO2 and iodine, Mater. Lett. 277 (2020), 128291, https://doi.org/10.1016/j.matlet.2020.128291.

[24] Y. Sang, Y. Cao, L. Wang, W. Yan, T. Chen, J. Huang, Y.-N. Liu, N-rich porous organic polymers based on Schiff base reaction for CO2 capture and mercury(II) adsorption, J. Colloid Interface Sci. 587 (2021) 121–130, https://doi.org/10.1016/j.jcis.2020.12.002.

[25] Y. Wang, M.J. Larsen, S. Rojas, M.-T. Sougrati, F. Jaouen, P. Ferrer, D. Gianolio, S. Berthon-Fabry, Influence of the synthesis parameters on the proton exchange membrane fuel cells performance of Fe–N–C aerogel catalysts, J. Power Sources 514 (2021), 230561, https://doi.org/10.1016/j.jpowsour.2021.230561.

[26] Y. Hu, J.O. Jensen, W. Zhang, S. Martin, R. Chenitz, C. Pan, W. Xing, N.J. Bjerrum, Q. Li, Fe 3 C-based oxygen reduction catalysts: synthesis, hollow spherical structures and applications in fuel cells, J. Mater. Chem. A 3 (2015) 1752–1760, https://doi.org/10.1039/C4TA03986F.

[27] O.S. Taskin, D. Dadashi-Silab, B. Kiskan, J. Weber, Y. Yagci, Highly efficient and reusable microporous Schiff base network polymer as a heterogeneous catalyst for CuAAC click reaction, Macromol. Chem. Phys. 216 (2015) 1746–1753, https://doi.org/10.1002/macp.201500141.

[28] M.G. Schwab, B. Fassbender, H.W. Spiess, A. Thomas, X. Feng, K. Müllen, Catalyst-free preparation of melamine-based microporous polymer networks through Schiff base chemistry, J. Am. Chem. Soc. 131 (2009) 7216–7217, https://doi.org/10.1021/ja902116f.

[29] G. Held, F. Venturini, D.C. Grinter, C. Stephens, A. Watts, P. Larkin, T. Richardson, S. Patel, M. Hillman, S. Scott, P. Ferrer, R. Arrigo, L. Deacon, W. Quevedo Garzon, K. Roy, A. Large, C. Stephens, A. Watts, P. Larkin, M. Hand, H. Wang, L. Pratt, J. J. Mudd, T. Richardson, S. Patel, M. Hillman, S. Scott, W.Q. Garzon, K. Roy, A. Large, C. Stephens, A. Watts, P. Larkin, M. Hand, H. Wang, L. Pratt, J.J. Mudd, T. Richardson, S. Patel, M. Hillman, S. Scott, Ambient-pressure endstation of the

versatile Soft X-ray (VerSoX) beamline at Diamond Light source, J. Synchrotron Radiat. 27 (2020) 1153–1166, https://doi.org/10.1107/S1600577520009157/VE5129SUP1.PDF.

[30] D.C. Grinter, F. Venturini, P. Ferrer, M.A. van Spronsen, R. Arrigo, W. Quevedo Garzon, K. Roy, A.I. Large, S. Kumar, G. Held, The versatile Soft X-ray (VerSoX) beamline at Diamond Light source, Synchrotron Radiat. News 35 (2022) 39–47, https://doi.org/10.1080/08940886.2022.2082181.

[31] A. Bonakdarpour, M. lefèvre, R. Yang, F.F. Jaouen, T. Dahn, J.-P. Dodelet, J. R. Dahn, M. Lefevre, R. Yang, F.F. Jaouen, T. Dahn, J.-P. Dodelet, J.R. Dahn, Impact of loading in RRDE experiments on Fe–N–C catalysts: two- or four-electron oxygen reduction? Electrochem. Solid State Lett. 11 (2008) B105, https://doi.org/10.1149/1.2904768.

[32] D. Malko, A. Kucernak, T. Lopes, In situ electrochemical quantification of active sites in Fe–N/C non-precious metal catalysts, Nat. Commun. 7 (2016), 13285, https://doi.org/10.1038/ncomms13285. http://www.nature.com/articles/ncomms13285#supplementary-information.

[33] D. Malko, T. Lopes, E. Symianakis, A.R. Kucernak, The intriguing poison tolerance of non-precious metal oxygen reduction catalysts, J. Mater. Chem. A. 4 (2016) 142–152, https://doi.org/10.1039/C5TA05794A.

[34] M. Primbs, Y. Sun, A. Roy, D. Malko, A. Mehmood, M.-T. Sougrati, P.-Y. Blanchard, G. Granozzi, T. Kosmala, G. Daniel, P. Atanassov, J. Sharman, C. Durante, A. Kucernak, D. Jones, F. Jaouen, P. Strasser, Establishing reactivity descriptors for platinum group metal (PGM)-free Fe–N–C catalysts for PEM fuel cells, Energy Environ. Sci. 13 (2020) 2480–2500, https://doi.org/10.1039/D0EE01013H.

[35] U.I. Kramm, J. Herranz, N. Larouche, T.M. Arruda, M. Lefèvre, F. Jaouen, P. Bogdanoff, S. Fiechter, I. Abs-Wurmbach, S. Mukerjee, J.P. Dodelet, Structure of the catalytic sites in Fe/N/C-catalysts for O 2-reduction in PEM fuel cells, Phys. Chem. Chem. Phys. 14 (2012) 11673–11688, https://doi.org/10.1039/c2cp41957b.

[36] C. Domínguez, F.J. Pérez-Alonso, M.A. Salam, S.A. Al-Thabaiti, M.A. Peña, F. J. García-García, L. Barrio, S. Rojas, Repercussion of the carbon matrix for the activity and stability of Fe/N/C electrocatalysts for the oxygen reduction reaction, Appl. Catal. B Environ. 183 (2016) 185–196, https://doi.org/10.1016/j.apcatb.2015.10.043.

[37] U.I. Kramm, M. Lefèvre, N. Larouche, D. Schmeisser, J.-P.P. Dodelet, Correlations between mass activity and physicochemical properties of Fe/N/C catalysts for the ORR in PEM fuel cell via 57Fe Mössbauer spectroscopy and other techniques, J. Am. Chem. Soc. 136 (2014) 978–985, https://doi.org/10.1021/ja410076f.

[38] J.F. Marco, J.R. Gancedo, A. Hernando, P. Crespo, C. Prados, J.M. González, N. Grobert, M. Terrones, D.R.M. Walton, H.W. Kroto, Mössbauer Study of Iron-Containing Carbon Nanotubes, 2002.

[39] R. Venegas, C. Zúñiga, J.H. Zagal, A. Toro-Labbé, J.F. Marco, N. Menéndez, K. Muñoz-Becerra, F.J. Recio, Fe3O4 templated pyrolyzed Fe−N−C catalysts.

[40] C. Domínguez, F.J. Pérez-Alonso, M. Abdel Salam, S.A. Al-Thabaiti, A.Y. Obaid, A. A. Alshehri, J.L. Gómez de la Fuente, J.L.G. Fierro, S. Rojas, On the relationship between N content, textural properties and catalytic performance for the oxygen reduction reaction of N/CNT, Appl. Catal. B Environ. 162 (2015) 420–429, https://doi.org/10.1016/j.apcatb.2014.07.002.

Understanding the role of N-functions and Fe3C on the ORR activity and mechanism, Chemelectrochem 9 (2022), e202200115, https://doi.org/10.1002/CELC.202200115.

[41] K. Kumar, L. Dubau, M. Mermoux, J. Li, A. Zitolo, J. Nelayah, F. Jaouen, F. Maillard, On the influence of oxygen on the degradation of Fe-N-C catalysts, Angew. Chem., Int. Ed. Engl. 59 (2020) 3235–3243, https://doi.org/10.1002/anie.201912451.

[42] P.G. Santori, F.D. Speck, J. Li, A. Zitolo, Q. Jia, S. Mukerjee, S. Cherevko, F. Jaouen, Effect of pyrolysis atmosphere and electrolyte pH on the oxygen reduction activity, stability and spectroscopic signature of FeN x moieties in Fe-N-C catalysts, J. Electrochem. Soc. 166 (2019), https://doi.org/10.1149/2.0371907jes. F3311–F3320.

[43] C. Domínguez, F.J.J. Pérez-Alonso, M.A.M.A. Salam, S.A. Al-Thabaiti, M.A.M. A. Peña, L. Barrio, S. Rojas, Effect of N/graphene catalysts for the oxygen reduction reaction in alkaline media, J. Mater. Chem. A. 3 (2015) 24487–24494, https://doi.org/10.1039/c5ta04355g.

[44] K. Artyushkova, A. Serov, S. Rojas-Carbonell, P. Atanassov, Chemistry of multitudinous active sites for oxygen reduction reaction in transition metal–nitrogen–carbon electrocatalysts, J. Phys. Chem. C 119 (2015) 25917–25928, https://doi.org/10.1021/acs.jpcc.5b07653.

[45] C. Zúñiga, C. Candia-Onfray, R. Venegas, K. Muñoz, J. Urra, M. Sánchez-Arenillas, J.F. Marco, J.H. Zagal, F.J. Recio, Elucidating the mechanism of the oxygen reduction reaction for pyrolyzed Fe-N-C catalysts in basic media, Electrochem. Commun. 102 (2019) 78–82, https://doi.org/10.1016/J.ELECOM.2019.04.005.

[46] I. Matanovic, K. Artyushkova, M.B. Strand, M.J. Dzara, S. Pylypenko, P. Atanassov, Core level shifts of hydrogenated pyridinic and pyrrolic nitrogen in the nitrogen-containing graphene-based electrocatalysts: in-plane vs edge defects, J. Phys. Chem. C 120 (2016) 29225–29232, https://doi.org/10.1021/acs.jpcc.6b09778.

[47] V. Armel, J. Hannauer, F. Jaouen, Effect of ZIF-8 crystal size on the O2 electro-reduction performance of pyrolyzed Fe–N–C catalysts, Catalysts 5 (2015) 1333–1351, https://doi.org/10.3390/catal5031333.

[48] A. Zitolo, V. Goellner, V. Armel, M.-T.T. Sougrati, T. Mineva, L. Stievano, E. Fonda, F. Jaouen, Identification of catalytic sites for oxygen reduction in iron- and nitrogen-doped graphene materials, Nat. Mater. 14 (2015) 937–942, https://doi.org/10.1038/nmat4367.

[49] S. Specchia, P. Atanassov, J.H. Zagal, Mapping transition metal–nitrogen–carbon catalyst performance on the critical descriptor diagram, Curr. Opin. Electrochem. 27 (2021), 100687, https://doi.org/10.1016/j.coelec.2021.100687.